Data report: calibration of XRF-estimated $CaCO_3$ along the Site U1338 splice[1]

Mitchell Lyle[2] and Jan Backman[3]

Chapter contents

[1]Lyle, M., and Backman, J., 2013. Data report: calibration of XRF-estimated $CaCO_3$ along the Site U1338 splice. *In* Pälike, H., Lyle, M., Nishi, H., Raffi, I., Gamage, K., Klaus, A., and the Expedition 320/321 Scientists, *Proc. IODP,* 320/321: Tokyo (Integrated Ocean Drilling Program Management International, Inc.). doi:10.2204/iodp.proc.320321.205.2013
[2]Department of Oceanography, Texas A&M University, College Station TX 77843, USA. mlyle@ocean.tamu.edu
[3]Department of Geological Sciences, Stockholm University, SE-10691 Stockholm, Sweden.

Abstract

We combined X-ray fluorescence (XRF) scan data from Integrated Ocean Drilling Program Expedition 321 Site U1338 and a set of 1060 discrete $CaCO_3$ measurements to calibrate a high-resolution XRF-estimated $CaCO_3$ profile for Site U1338. In this data report, we describe the method of calibration, using normalized median-scaled XRF data and discrete $CaCO_3$ measurements. A subset of ~¾ of the discrete measurements was used to calibrate the XRF scan, and the quality of the calibration was checked with the remainder of the discrete data. Based upon the check data, the calibrated XRF $CaCO_3$ estimate is within ±5% of the independent discrete measurements (1 standard deviation). The calibrated XRF $CaCO_3$ estimate provides, for the first time, a carbonate profile for the middle Miocene–Holocene with a resolution of ~2 k.y. for the uppermost 60 compressed meters composite depth below seafloor and ≤1 k.y. resolution in the rest of the sediment section.

Introduction

A primary objective of the Integrated Ocean Drilling Program (IODP) Pacific Equatorial Age Transect (PEAT) project is to study the evolution of Earth systems in the equatorial Pacific from 50 to 0 Ma (see the **"Expedition 320/321 summary"** chapter [Pälike et al., 2010]). This objective requires the production of continuous sediment records sampled frequently enough to resolve the effects of orbital forcing. It has long been known that the burial of $CaCO_3$ in the equatorial Pacific has varied on all timescales driven by climate-related changes in ocean chemistry and/or productivity (Hays et al., 1969; van Andel and Moore, 1974; Mayer et al., 1986; Lyle, 2003). X-ray fluorescence (XRF) scanning, because it is a fast, low-cost measurement, can potentially measure frequently enough to achieve sample spacings of <5 k.y. and resolve an orbitally forced signal on 10 m.y. time frames. We report here the construction of a $CaCO_3$ profile for the 414 m thick sediment column at Site U1338 based on calibrated XRF measurements.

Site U1338 (2°30.469′N, 117°58.178′W; 4200 m water depth) (Fig. **F1**) is on 18 Ma ocean crust buried by 414 m of pelagic sediment (see the **"Site U1338"** chapter [Expedition 320/321 Scientists, 2010b]). The sediment drapes over the topography so that the ~200 m abyssal hill relief on the basement is still visible at the sea-

doi:10.2204/iodp.proc.320321.205.2013

floor despite the 400 m of sediment cover (Tominaga et al., 2011).

Lyle et al. (2012) presents a method to condition XRF data for later calibration that works well for carbonate sediment from the equatorial Pacific. The methodology (1) scales the range of individual element XRF peak areas to better match the range of sediment elemental concentrations by scaling the median peak area to the median of measured bulk sediment composition, followed by (2) normalization of the sediment composition to 100% assuming a set of model sediment components.

The scaling process is needed because characteristic X-ray production by different elements depends not only on an element's bulk concentration in sediment but also on its efficiency at absorbing and fluorescing X-rays. The normalization process is needed because XRF is a volume measurement, not a mass measurement. Each XRF measurement illuminates a certain volume of sediment, but the mass of sediment illuminated in different samples may not be the same because of porosity. The illumination volume is also dependent on composition, which affects penetration efficiency and absorption characteristics of different X-ray energies (Tjallingii et al., 2007). The composition effect will most strongly affect estimated composition if the surface region has a different composition than layers below. Because of the volume measurement problem, raw elemental peak areas are affected by both porosity and composition (Fig. **F2**). These volume effects create biases between individual measurements as well as systematic offsets over a large sediment column. Normalizing total component percentages to 100% eliminates much of this effect.

In this paper, we show how the XRF data from Site U1338 were calibrated and how errors were estimated, and we tabulate both the calibration data set and the XRF-estimated $CaCO_3$. The XRF data set has a time resolution between samples of ~2 k.y. in the uppermost Miocene to Holocene sediments and ≤1 k.y. in the sediment section below. The time resolution changes because of slower sedimentation in the upper section of Site U1338 (see the **"Site U1338"** chapter [Expedition 320/321 Scientists, 2010b])

Methods

XRF scan data were acquired at Texas A&M University (USA), and the $CaCO_3$ analyses were done at Stockholm University (Sweden).

XRF data acquisition

XRF scans were done using the Ocean Drilling and Sustainable Earth Science (ODASES) XRF scanning facility at the IODP Gulf Coast Repository (GCR) in College Station, Texas (USA) (**odases.tamu.edu/research-facilities/xrf-request**), using a third-generation Avaatech XRF scanner with a Canberra X-PIPS (passivated implanted planar silicon) silicon drift detector (SDD), Model SXD 15C-150-500 150 eV resolution X-ray detector. The XRF scanner is configured to analyze split sediment core halves for elements between Al and U in the periodic table. The X-ray tube and detector apparatus are mounted on a moving track so that multiple spots at different depths can be analyzed on a split core in a single scanning run and multiple scans with different settings can be automatically programmed. Scan parameters are controlled by the operator, including X-ray tube current, tube voltage, measurement time (live time), X-ray filters used, and area of X-ray illumination. The downcore position step is also programmed and is precise to 0.1 mm. A basic description of first and second generation Avaatech scanners are given in Richter et al. (2006). The ODASES scanner is a third-generation Avaatech scanner.

For the Site U1338 XRF scans, each core section was removed from refrigeration at least 2 h before scanning and scraped to clean the split core surface. The surface was covered with 4 µm thick Ultralene plastic film (SPEX Centriprep, Inc.) to prevent contamination of the X-ray detector. Measurements were taken at 2.5 cm intervals, and separate scans at two voltages were done. One scan was performed at 10 kV for the elements Al, Si, S, Cl, K, Ca, Ti, Mn, and Fe, and a repeat scan was performed at 50 kV for Ba. The voltage used for elements measured is determined by the energy needed to excite the appropriate characteristic X-rays. The X-ray illumination area was set at 1.0 cm in the downcore direction and 1.2 cm in the cross-core direction, and the scan was run down the center of the split core half. Both scans were done with an X-ray tube current of 2 mA. Settings used for the Site U1338 10 kV XRF scans are 2 mA tube current, no filter, and a detector live time of 20 s; for the 50 kV scan, the settings are 2 mA current, Cu filter, and a detector live time of 10 s.

Further details about the XRF scanning procedure and reproducibility can be found in **Lyle et al.** (2012).

$CaCO_3$ analyses

Calcium carbonate concentrations were determined using a Model 5012 UIC coulometer. Samples were freeze-dried, ground to dry powder, and stored in a desiccator prior to analysis. In sediment samples with carbonate contents in excess of 25%, ~30 mg of the sediment powder was placed in a Teflon cup and weighed using a Sartorius MC5 microbalance, with a

standard deviation of better than ±1 µg and a linearity of better than ±2 µg within 500 mg. The cup with its sediment powder was placed in the coulometer sample tube, and then 2 mL 2 M HCl was added, drenching the entire cup and the sediment powder in it. The operation of the coulometer followed procedures recommended by the instrument manufacturer. A few standards of pure calcium carbonate (Merck 2060, 99.95%–100.05% $CaCO_3$) were analyzed before and after the daily runs of sediment samples. Coulometer $CaCO_3$ values were recalculated using a calibration algorithm described by Mörth and Backman (2011), based on analyses of 460 pure calcium carbonate standards. They also demonstrated that in order to generate a precision of ±0.8%, at least 7 mg of 100% calcite is needed. Mörth and Backman (2011) show that a sample size of 35 mg will meet the ±0.8% criterion in all sediment samples ranging from 100% to 20% carbonate content. A sample containing only 10% carbonate will need a sample size of 70 mg in order to meet the ±0.8% criterion. The uncertainty increases in samples having <10% calcium carbonate.

Calibration of XRF data to $CaCO_3$ measurements

The XRF normalized median-scaled (NMS) $CaCO_3$ data from **Lyle et al.** (2012) was used for calibration and verification. Although the scaling and normalization steps make the NMS data more linear with respect to the calibration, they are not a calibration. The NMS data were calibrated with the $CaCO_3$ measurements from Stockholm University listed in Table **T1** to become true estimates of $CaCO_3$ wt%.

We used 255 $CaCO_3$ measurements as the calibration data set for the Site U1338 splice and reserved the remaining $CaCO_3$ analyses as the check data set. The number in the calibration data set was determined by preliminary calibration trials. We made certain there was a range of $CaCO_3$ wt% at all depths. Where there appeared to be systematic offsets, we added more calibration data to help the calibration better conform to the data set. The final calibration is from the linear regression shown in Figure **F3** with an R^2 of 0.87:

$$\text{XRF } CaCO_3 = NMS_{CaCO3} \times 1.0241 - 7.904,$$

where NMS_{CaCO3} is the XRF NMS $CaCO_3$ component as reported in **Lyle et al.** (2012) and XRF $CaCO_3$ is the XRF estimate of carbonate content. XRF $CaCO_3$ estimates are listed in Table **T2.**

The calibration line is offset from the 1:1 line in Figure **F3** because the NMS model used to precondition the Site U1338 XRF data is biased slightly high with respect to the actual $CaCO_3$ measurements. Nevertheless, the uncalibrated data do a reasonable job of estimating differences downcore, as the difference between the NMS model $CaCO_3$ and measured $CaCO_3$ stays reasonably constant. The slope of the calibration line, in other words, is close to 1.

The remaining 850 $CaCO_3$ analyses were used to check the quality of the XRF $CaCO_3$ estimate. The locations of both check data and calibration data are shown with a profile of $CaCO_3$ estimated by XRF in Figure **F4,** and differences between paired $CaCO_3$ measurements and their XRF estimates are shown in Figure **F5.** Assuming a normal distribution, the standard deviation is ±4.98%. However, the distribution is more peaked than a Gaussian distribution. The data are marked by a few large mismatches, typically where there are large changes in $CaCO_3$ wt% over short depth intervals.

The difference data have high kurtosis (more near-correct values than expected by a Gaussian distribution). Although 1 standard deviation is ±4.98%, 76% of the data is between ±5% of the correct value, rather than the expected 67%. We find that the highest differences between measured $CaCO_3$ and the XRF estimate occur where there are rapid changes in $CaCO_3$ content, suggesting that the greater differences between the two do not entirely represent error but also include actual differences in depth-matched samples when rates of change are high. Such differences might occur either where there are slight mismatches in depth or where there are significant differences between the sample composition near the center (and surface) of the split core where the XRF measurements were taken, versus near the edge (and below the surface) of the core where the discrete samples were taken. Alternately, the large tails may represent systematic mismatches at the extrema of the calibration. Examination of the data shows that the largest values clearly are "fliers" (i.e., rare cases where one data point was significantly mislabeled in depth or for some reason failed to be measured accurately).

We also find a slight but systematic positive trend in the differences between measured and estimated $CaCO_3$ versus depth, suggesting that a small uncorrected porosity effect is still contained in the XRF estimate or that the slope of the calibration should be somewhat greater. Figure **F6** shows the difference between measured and estimated $CaCO_3$ versus depth in the core. For 0–100 compressed meters composite depth below seafloor (cmcd; using the CCSF-B

method; see the "Methods" chapter [Expedition 320/321 Scientists, 2010a]), there is a systematic bias in the XRF estimate so that the XRF estimate averages 4% higher than the measured values with large scatter. Below 300 cmcd, the XRF estimate is systematically about 3%–4% lower than the measured values. This bias must be kept in mind but does not affect relative differences between samples on the 100 m scale.

Differences between measured and estimated $CaCO_3$ are also somewhat smaller below 300 cmcd, but it is unclear whether this reflects lower errors because the $CaCO_3$ content is less variable and the likelihood of calibration sample mismatches is less or whether the higher variability near the surface results from poorer ability to correct for porosity bias in the XRF data in the high porosity zone. Further work will help to better understand the porosity effect on the calibration.

Discussion: high-resolution $CaCO_3$ profile from Site U1338

Calibrating the XRF measurements with discrete $CaCO_3$ data makes it possible to examine high-resolution variability in the carbon cycle since the late early Miocene. Although the crustal age at Site U1338 is ~18 Ma, variable sedimentation at the base of the core, including additions of hydrothermal sediment as well as unresolved issues about the core splice, make us hesitant to interpret the record below 16 Ma. Above that level, sedimentation responds to a large-scale pattern common to most drill sites in the equatorial Pacific. Sedimentation increases as the site is carried to the Equator by Pacific plate movement and then decreases as the site moves away from the Equator. The crust at Site U1338 formed at ~1.5°S and crossed the Equator at ~11.5 Ma, where sedimentation rates were ~30 m/m.y. (see the "Site U1338" chapter [Expedition 320/321 Scientists, 2010b]). Sedimentation rates slowed dramatically to ~12 m/m.y. at ~4.65 Ma, as Site U1338 passed 1.5°N. These changes in sedimentation make the resolution of $CaCO_3$ sampling above 4.65 Ma ~2 k.y. between samples, whereas the deeper record has a time resolution of <1 k.y. Responses to orbital forcing should be easily resolved, provided that the high-resolution variability in the profile reflects changes in sediment chemistry and not measurement variability.

Is the high-resolution XRF $CaCO_3$ estimate signal or noise?

High-resolution discrete $CaCO_3$ measurements were taken every 10 cm between 180 and 230 cmcd versus a spacing of roughly 75 cm in other intervals. Even in the highly sampled interval, XRF measurements are a factor of 4 higher in resolution than the discrete sampling. In Figure F7 the discrete and XRF depth series are compared to each other to determine whether the higher resolution XRF estimate actually represents $CaCO_3$ variations. The discrete $CaCO_3$ and XRF $CaCO_3$ profiles strongly resemble each other, despite the coarser discrete sample spacing. All of the major features and most of the minor features in the XRF $CaCO_3$ profile are reproduced by the discrete $CaCO_3$ data. A few points show significant mismatches between discrete and XRF $CaCO_3$. In each case, the difference appears to be either a sample with the wrong depth or a sample where there is an actual difference in $CaCO_3$ caused by the different sample positions of each measurement.

Figure F7 also shows the gamma ray attenuation (GRA) bulk density profile from Site U1338 (see Fig. F29 in the "Site U1338" chapter [Expedition 320/321 Scientists, 2010b]). The GRA profile is another way to estimate high-resolution $CaCO_3$ trends based on the well-known relationship between $CaCO_3$ content and bulk density in equatorial Pacific sediment (Lyle and Dymond, 1976; Mayer, 1991; Lyle et al., 1995). In order to make $CaCO_3$ estimates from bulk density, it is first necessary to "decompact" the sediment (i.e., remove the porosity decrease caused by increasing the sedimentary overburden) (Mayer, 1991). In short intervals such as the one shown in Figure F7, decompaction can be ignored when comparing trends.

Small features not clearly resolved in the 10 cm discrete sampling appear in both the GRA bulk density profile and the XRF $CaCO_3$ estimate. For example, in the interval between 206 and 207.5 cmcd, both bulk density and XRF clearly identify an intermediate peak between the initial and final peaks. The discrete data are ambiguous about the middle peak, as it was sampled by only 1 data point. The higher resolution XRF estimate of $CaCO_3$ thus contains an actual signal from the sediment and not sample-to-sample noise.

Large-scale features of the Site U1338 $CaCO_3$ profile

Large-scale chronostratigraphic $CaCO_3$ events have been previously identified in the equatorial Pacific and are the basis for the Neogene equatorial Pacific seismic stratigraphy (Mayer et al., 1986). One of the objectives of Expedition 320/321 was to better identify these events and put them into a modern chronostratigraphic framework.

Figure F8 is an illustration of the Site U1338 $CaCO_3$ curve and identifies important low $CaCO_3$ intervals by blue shading. There are three potential processes that cause low $CaCO_3$—additional dissolution by more corrosive bottom water, low carbonate productivity, or extreme relative increases in productivity by diatoms (a bio-SiO_2 producer; e.g., Kemp and Baldauf, 1993). Further work is being done to determine how each process contributes to each low-$CaCO_3$ interval. Nevertheless, we note that low-$CaCO_3$ intervals have been identified as causes of the distinct Neogene seismic stratigraphy of the equatorial Pacific (Mayer et al., 1986; Bloomer et al., 1995) and can be correlated for 3000 km across the equatorial Pacific (Tominaga et al., 2011). In Figure F8 we use a revision of the Site U1338 age model (J. Backman and J. Baldauf, unpubl. data) to correlate the Mayer et al. (1985) central equatorial Pacific seismic stratigraphy to the Site U1338 carbonate curve.

Inspection of Figure F8 shows that $CaCO_3$ content varies at multiple age scales. The high-resolution "chatter" in the record represents the ±20% variation in $CaCO_3$ associated with orbitally forced climate change. This scale of variation will be investigated more fully in the future as the age models are orbitally tuned. The larger scale events shown in Figure F8 have amplitudes of 40% or greater and last for varying amounts of time, as little as 300 k.y. to ~2 m.y. These low-$CaCO_3$ events mark significant reorganizations of the equatorial Pacific that are important to understand, as they probably do not represent linear responses to orbital forcing. There are now new tools to investigate their history with the newly collected near-continuous sediment records from Expedition 320/321 and new high-resolution analyses using calibrated XRF scans.

Conclusions

We used XRF measurement of Ca peak area and discrete $CaCO_3$ analyses from Site U1338 to calibrate a high-resolution $CaCO_3$ profile along the Site U1338 splice. Data spacing of 2.5 cm results in analyses at ~2 k.y. age spacing from 0 to 58 cmcd (0 to 4.65 Ma) and ~ 1 k.y. spacing or less below, from 4.65 to >16 Ma. By comparing discrete data, XRF data, and the GRA bulk density profile, we find that the high-resolution XRF profile represents changes in sedimentary $CaCO_3$ content and not measurement variability. We find that the XRF $CaCO_3$ estimate is typically within 5% of the discrete measurements, but that there is a minor depth-related bias to the XRF $CaCO_3$ estimate. This new high-resolution $CaCO_3$ profile will allow further work to probe the changes in the Neogene carbon cycle.

Acknowledgments

We thank the Expedition 320/321 Scientific Party, IODP, and the IODP GCR for providing samples and data for this report and for all the effort expended to properly collect and archive the Site U1338 sediment cores. The paper was improved by a review by Dr. Ursula Röhl. We also acknowledge the ODASES program at Texas A&M University for acquiring the Avaatech XRF scanner for the GCR. Scanning and analysis were paid for by a United States Advisory Committee for Scientific Ocean Drilling (USAC) postcruise grant and by National Science Foundation (NSF) grant OCE-0962184 to M. Lyle.

References

Bloomer, S.F., Mayer, L.A., and Moore, T.C., Jr., 1995. Seismic stratigraphy of the eastern equatorial Pacific Ocean: paleoceanographic implications. *In* Pisias, N.G., Mayer, L.A., Janecek, T.R., Palmer-Julson, A., and van Andel, T.H. (Eds.), *Proc. ODP, Sci. Results,* 138: College Station, TX (Ocean Drilling Program), 537–553. **doi:10.2973/odp.proc.sr.138.128.1995**

Expedition 320/321 Scientists, 2010a. Methods. *In* Pälike, H., Lyle, M., Nishi, H., Raffi, I., Gamage, K., Klaus, A., and the Expedition 320/321 Scientists, *Proc. IODP,* 320/321: Tokyo (Integrated Ocean Drilling Program Management International, Inc.). **doi:10.2204/iodp.proc.320321.102.2010**

Expedition 320/321 Scientists, 2010b. Site U1338. *In* Pälike, H., Lyle, M., Nishi, H., Raffi, I., Gamage, K., Klaus, A., and the Expedition 320/321 Scientists, *Proc. IODP,* 320/321: Tokyo (Integrated Ocean Drilling Program Management International, Inc.). **doi:10.2204/iodp.proc.320321.110.2010**

Hays, J.D., Saito, T., Opdyke, N.D., and Burckle, L.H., 1969. Pliocene-Pleistocene sediments of the equatorial Pacific: their paleomagnetic, biostratigraphic, and climatic record. *Geol. Soc. Am. Bull.,* 80(8):1481–1514. **doi:10.1130/0016-7606(1969)80[1481:PSOTEP]2.0.CO;2**

Kemp, A.E.S., and Baldauf, J.G., 1993. Vast Neogene laminated diatom mat deposits from the eastern equatorial Pacific Ocean. *Nature (London, U. K.),* 362(6416):141–144. **doi:10.1038/362141a0**

Lyle, M., 2003. Neogene carbonate burial in the Pacific Ocean. *Paleoceanography,* 18(3):1059. **doi:10.1029/2002PA000777**

Lyle, M., Dadey, K.A., and Farrell, J.W., 1995. The late Miocene (11–8 Ma) eastern Pacific carbonate crash: evidence for reorganization of deep-water circulation by the closure of the Panama gateway. *In* Pisias, N.G.,

Mayer, L.A., Janecek, T.R., Palmer-Julson, A., and van Andel, T.H. (Eds.), *Proc. ODP, Sci. Results,* 138: College Station, TX (Ocean Drilling Program), 821–838. **doi:10.2973/odp.proc.sr.138.157.1995**

Lyle, M., Olivarez Lyle, A., Gorgas, T., Holbourn, A., Westerhold, T., Hathorne, E., Kimoto, K., and Yamamoto, S., 2012. Data report: raw and normalized elemental data along the Site U1338 splice from X-ray fluorescence scanning. *In* Pälike, H., Lyle, M., Nishi, H., Raffi, I., Gamage, K., Klaus, A., and the Expedition 320/321 Scientists, *Proc. IODP,* 320/321: Tokyo (Integrated Ocean Drilling Program Management International, Inc.). **doi:10.2204/iodp.proc.320321.203.2012**

Lyle, M.W., and Dymond, J., 1976. Metal accumulation rates in the southeast Pacific—errors introduced from assumed bulk densities. *Earth Planet. Sci. Lett.,* 30(2):164–168. **doi:10.1016/0012-821X(76)90242-9**

Mayer, L.A., 1991. Extraction of high-resolution carbonate data for palaeoclimate reconstruction. *Nature (London, U. K.),* 352(6331):148–150. **doi:10.1038/352148a0**

Mayer, L.A., Shipley, T.H., Theyer, F., Wilkens, R.H., and Winterer, E.L., 1985. Seismic modeling and paleoceanography at Deep Sea Drilling Project Site 574. *In* Mayer, L., Theyer, F., Thomas, E., et al., *Init. Repts. DSDP,* 85: Washington, DC (U.S. Govt. Printing Office), 947–970. **doi:10.2973/dsdp.proc.85.132.1985**

Mayer, L.A., Shipley, T.H., and Winterer, E.L., 1986. Equatorial Pacific seismic reflectors as indicators of global oceanographic events. *Science,* 233(4765):761–764. **doi:10.1126/science.233.4765.761**

Mörth, C.-M., and Backman, J., 2011. Practical steps for improved estimates of calcium carbonate concentrations in deep sea sediments using coulometry. *Limnol. Oceanogr.: Methods,* 9:565–570. **doi:10.4319/lom.2011.9.565**

Pälike, H., Nishi, H., Lyle, M., Raffi, I., Gamage, K., Klaus, A., and the Expedition 320/321 Scientists, 2010. Expedition 320/321 summary. *In* Pälike, H., Lyle, M., Nishi, H., Raffi, I., Gamage, K., Klaus, A., and the Expedition 320/321 Scientists, *Proc. IODP,* 320/321: Tokyo (Integrated Ocean Drilling Program Management International, Inc.). **doi:10.2204/iodp.proc.320321.101.2010**

Richter, T.O., van der Gaast, S., Koster, B., Vaars, A., Gieles, R., de Stigter, H.C., De Haas, H., and van Weering, T.C.E., 2006. The Avaatech XRF Core Scanner: technical description and applications to NE Atlantic sediments. *In* Rothwell, R.G. (Ed.), *New Techniques in Sediment Core Analysis*. Geol. Soc. Spec. Publ., 267(1):39–50. **doi:10.1144/GSL.SP.2006.267.01.03**

Tjallingii, R., Röhl, U., Kölling, M., and Bickert, T., 2007. Influence of the water content on X-ray fluorescence core-scanning measurements in soft marine sediments. *Geochem., Geophys., Geosyst.,* 8(2):Q02004. **doi:10.1029/2006GC001393**

Tominaga, M., Lyle, M., and Mitchell, N., 2011. Seismic interpretation of pelagic sedimentation regimes in the 18–53 Ma eastern equatorial Pacific: basin-scale sedimentation and infilling of abyssal valleys. *Geochem., Geophys., Geosyst.,* 12:Q03004. **doi:10.1029/2010GC003347**

van Andel, T.H., and Moore, T.C., Jr., 1974. Cenozoic calcium carbonate distribution and calcite compensation in the central equatorial Pacific Ocean. *Geology,* 2(2):87–92. **doi:10.1130/0091-7613(1974)2<87:CCCDAC>2.0.CO;2**

Wilkens, R.H., Dickens, G.R., Tian, J., Backman, J., and the Expedition 320/321 Scientists, 2013. Data report: revised composite depth scales for Sites U1336, U1337, and U1338. *In* Pälike, H., Lyle, M., Nishi, H., Raffi, I., Gamage, K., Klaus, A., and the Expedition 320/321 Scientists, *Proc. IODP,* 320/321: Tokyo (Integrated Ocean Drilling Program Management International, Inc.). **doi:10.2204/iodp.proc.320321.209.2013**

Initial receipt: 14 December 2011
Acceptance: 24 January 2013
Publication: 5 April 2013
MS 320321-205

Figure F1. Maps of Site U1338, located on 18 Ma crust formed at the East Pacific Rise. Plate tectonic movement of the Pacific plate carried Site U1338 within 0.5° of the Equator between 13 and 8 Ma. (From the **"Expedition 320/321 summary"** chapter [Pälike et al., 2010].)

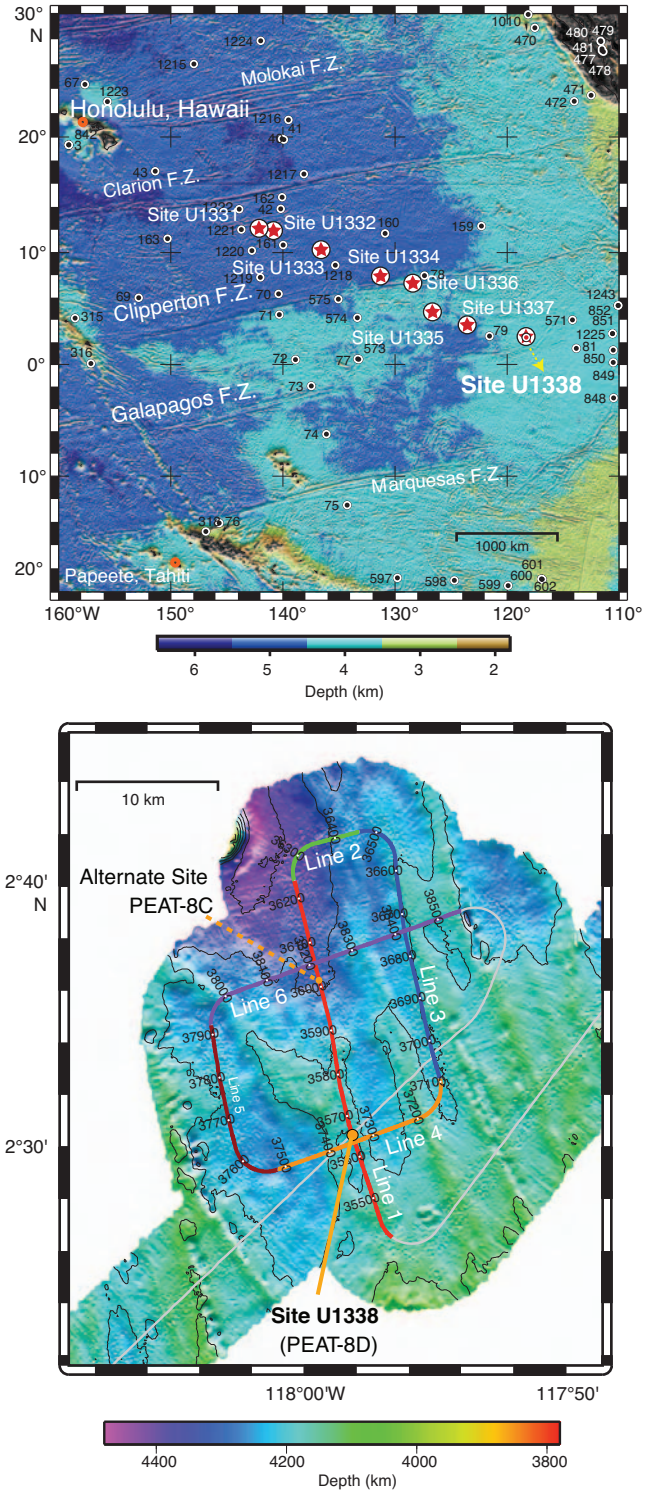

Figure F2. Raw X-ray fluorescence (XRF) Ca peak area profile graphed with discrete $CaCO_3$ wt% at Site U1338. Because XRF is a volume measurement and not a mass measurement, the raw Ca peak areas increase systematically with depth because the porosity of the sediment decreases and the illuminated mass of sediment in each measurement increases.

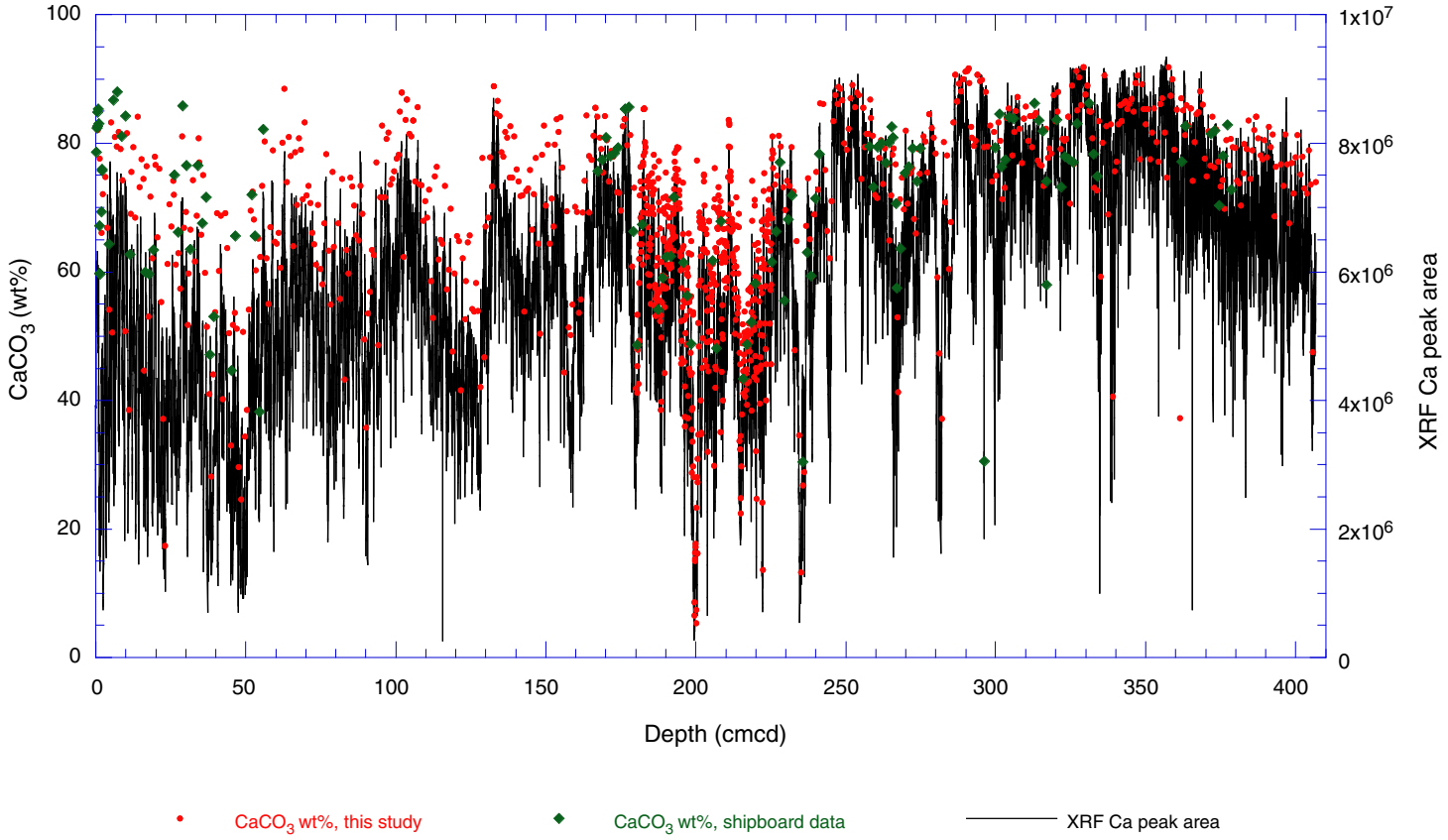

Figure F3. Normalized median-scaled (NMS) X-ray fluorescence (XRF) $CaCO_3$ plotted against 255 discrete $CaCO_3$ analyses from the same depth intervals at Site U1338. The red line shows the linear least-squares fit to the data, and the black dashed line represents the perfect fit.

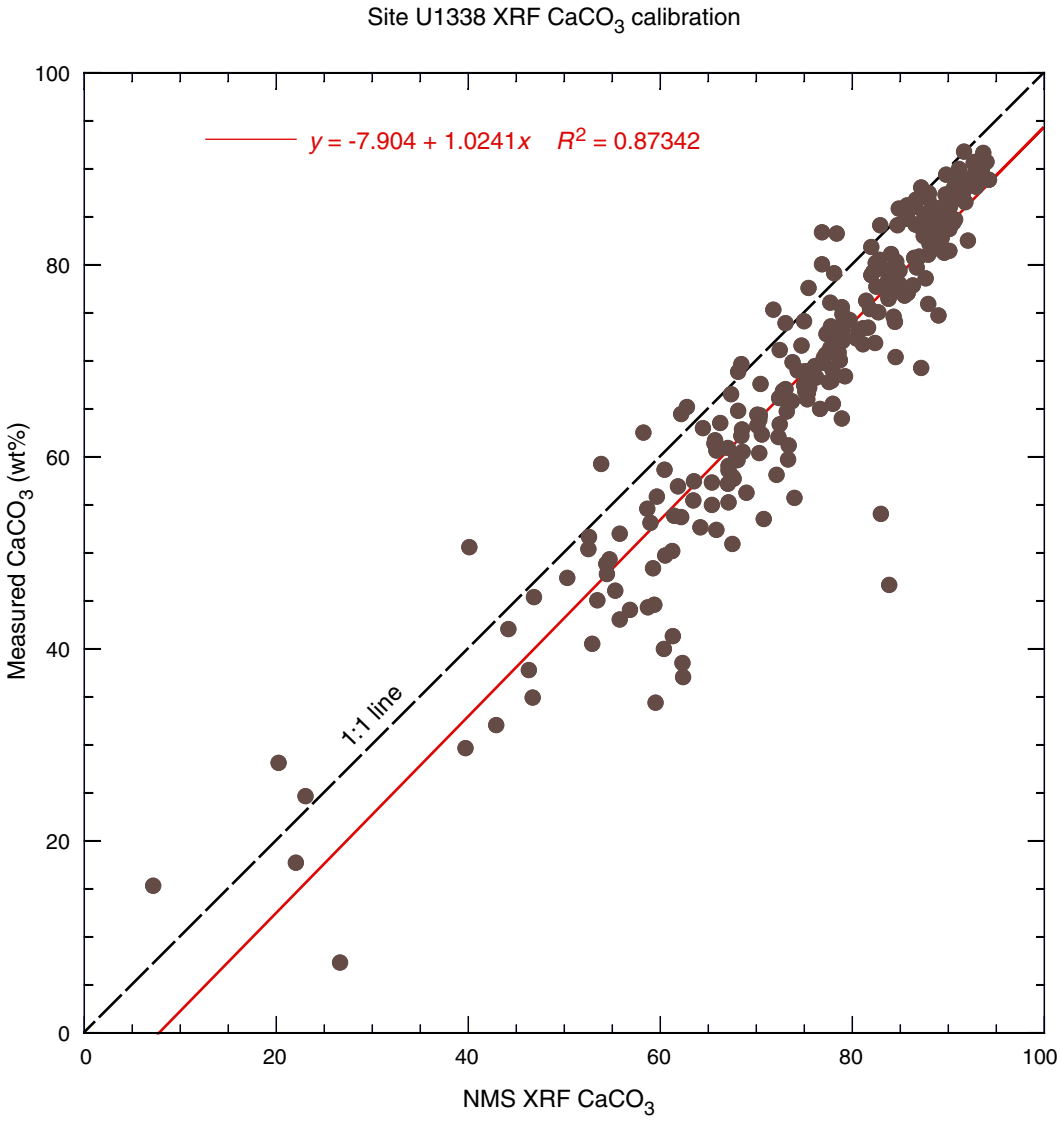

Figure F4. Site U1338 carbonate profile. Calibration data are the discrete $CaCO_3$ calibration data set, and check data are the discrete $CaCO_3$ check data set. XRF = X-ray fluorescence.

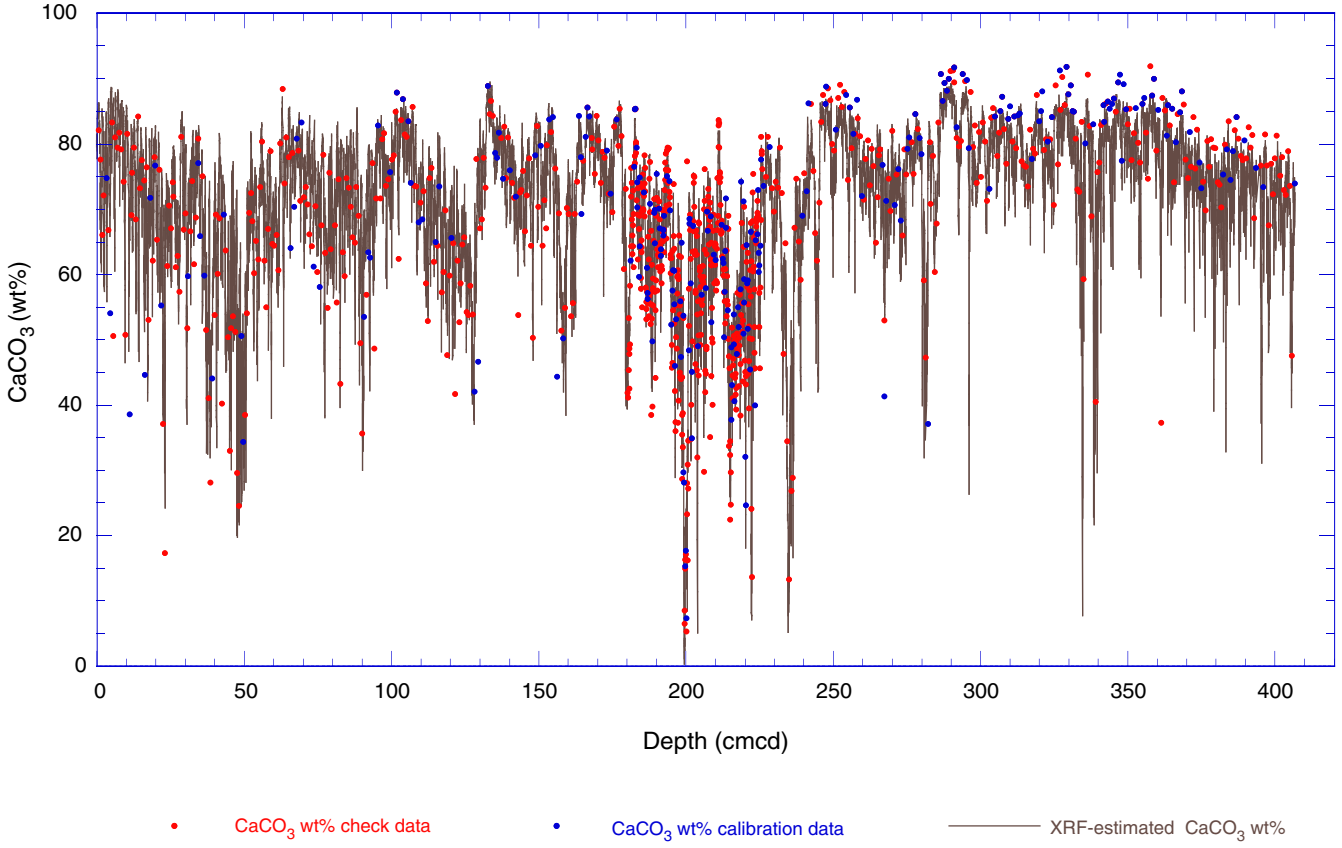

Figure F5. Histogram of differences between measured and XRF-estimated $CaCO_3$ at the same measurement depths, Site U1338. 76% of the XRF estimates are within 5% of the measured $CaCO_3$ value. RMS = root mean square, XRF = X-ray fluorescence.

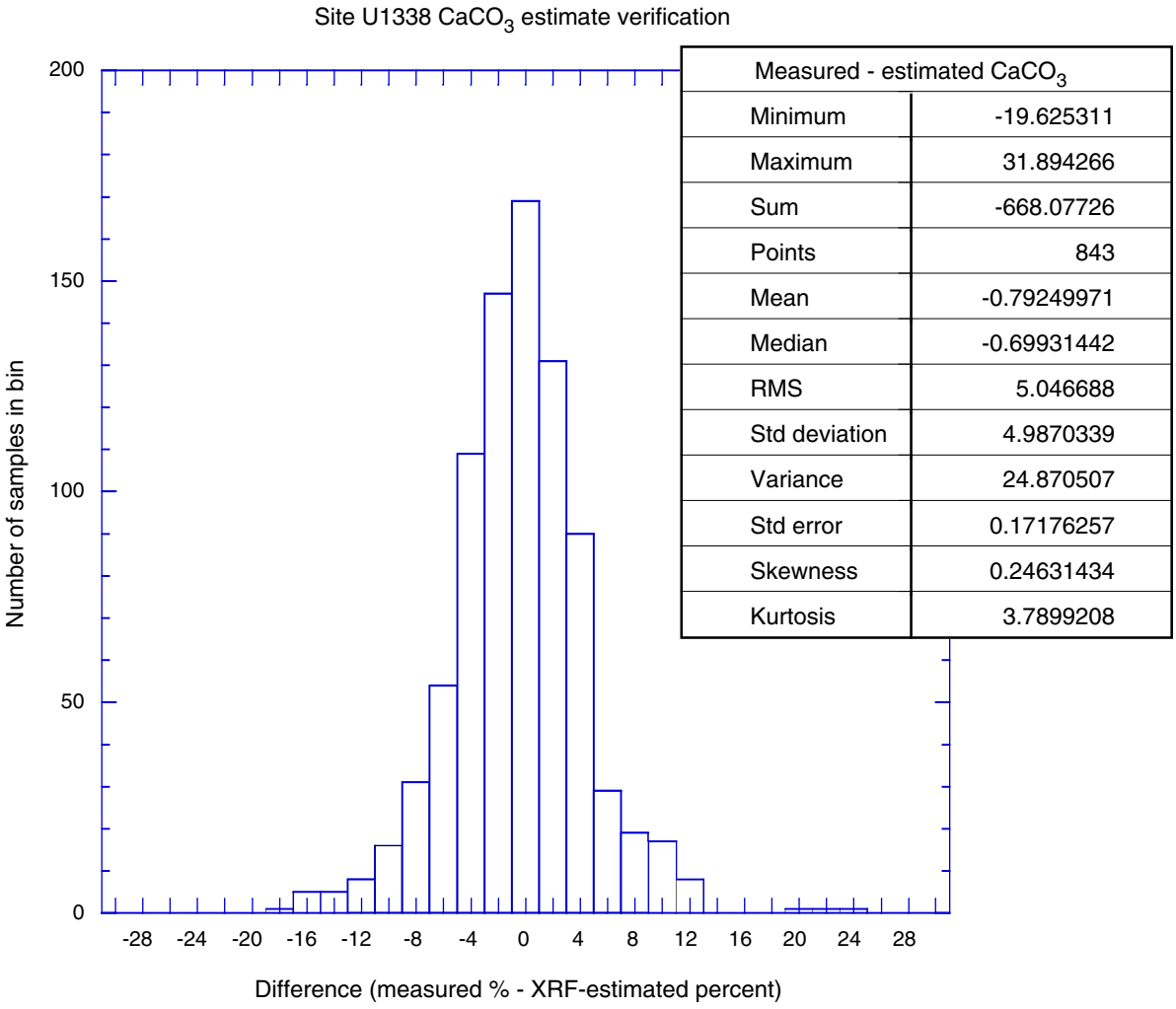

Figure F6. Bias in X-ray fluorescence (XRF) estimate of $CaCO_3$ with depth in the Site U1338 sediment section. XRF $CaCO_3$ estimates tend to be higher than measured $CaCO_3$ in the 0–150 cmcd interval but tend to be below the measured $CaCO_3$ in the interval below 300 cmcd.

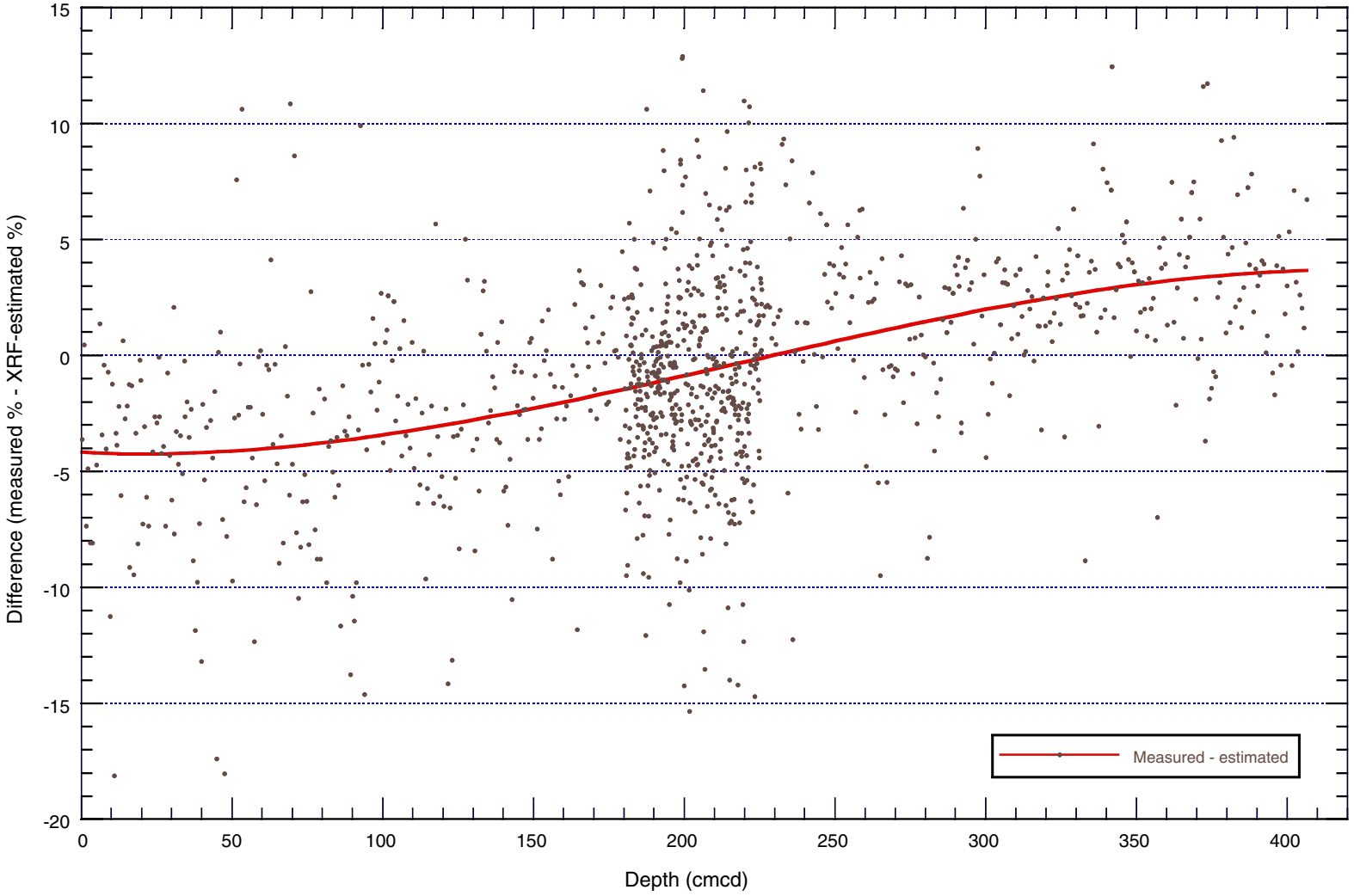

Figure F7. Detail of Site U1338 X-ray fluorescence (XRF) $CaCO_3$ profile in the section where $CaCO_3$ was measured at 10 cm intervals. The gamma ray attenuation (GRA) bulk density profile over the same interval is also shown, as bulk density in equatorial Pacific sediment is strongly correlated to carbonate content. All three data sets exhibit the same high-frequency variation, suggesting that the noise in the XRF estimate is small. Calibration data are the discrete $CaCO_3$ calibration data set, and check data are the discrete $CaCO_3$ check data set.

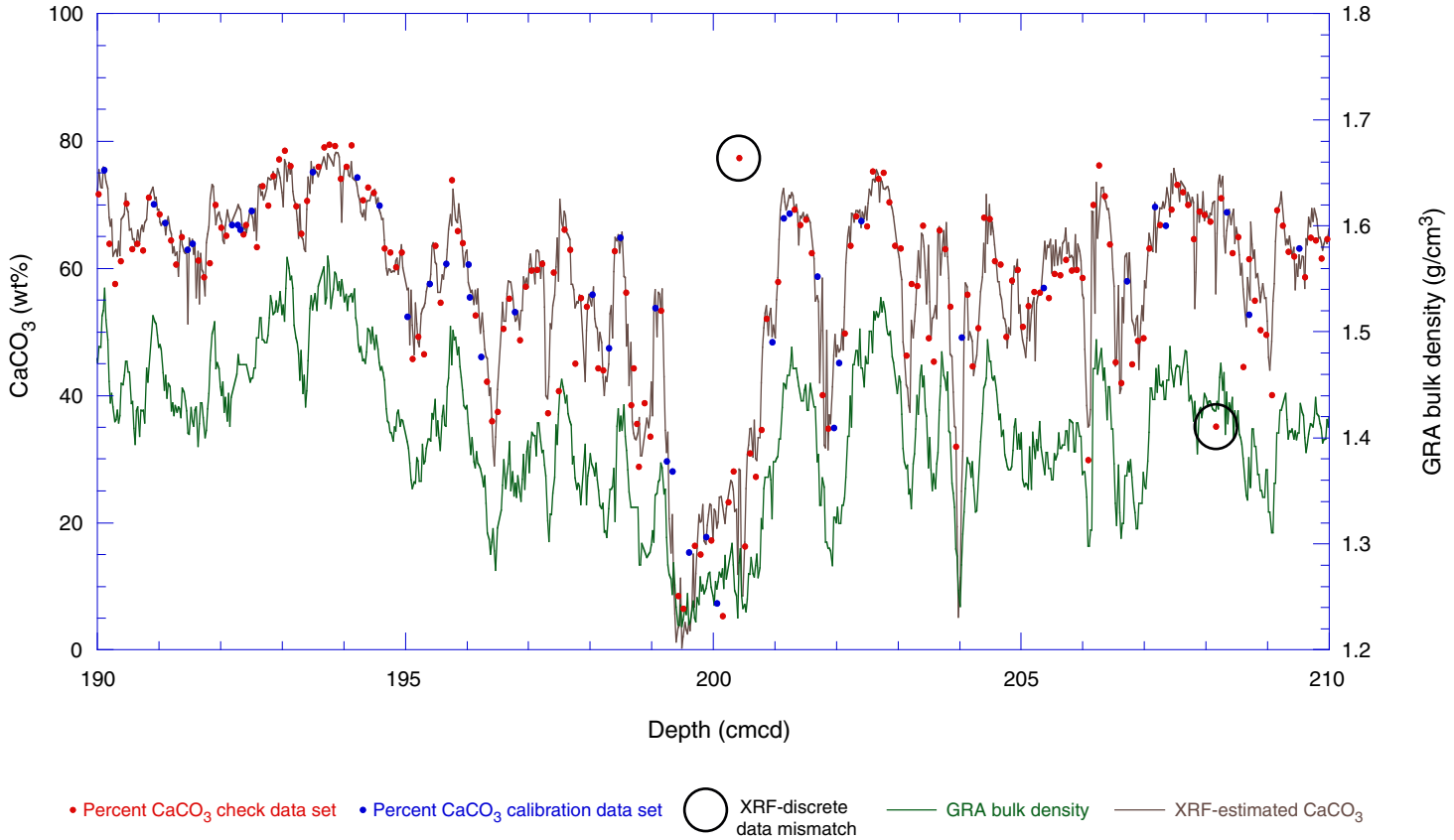

Figure F8. Low $CaCO_3$ transients in the Site U1338 record. Blue ages for blue-shaded intervals use an unpublished revision of the Site U1338 chronostratigraphy (J. Backman and J. Baldauf, unpubl. data). Black names and dates refer to the central Pacific Neogene seismic stratigraphy of Mayer et al. (1985). Dates for the seismic intervals are based on Site 574 biostratigraphy, updated to the Pacific Equatorial Age Transect age model (see the **"Methods"** chapter [Expedition 320/321 Scientists, 2010a]). Calibration data are the discrete $CaCO_3$ calibration data set, and check data are the discrete $CaCO_3$ check data set. XRF = X-ray fluorescence.

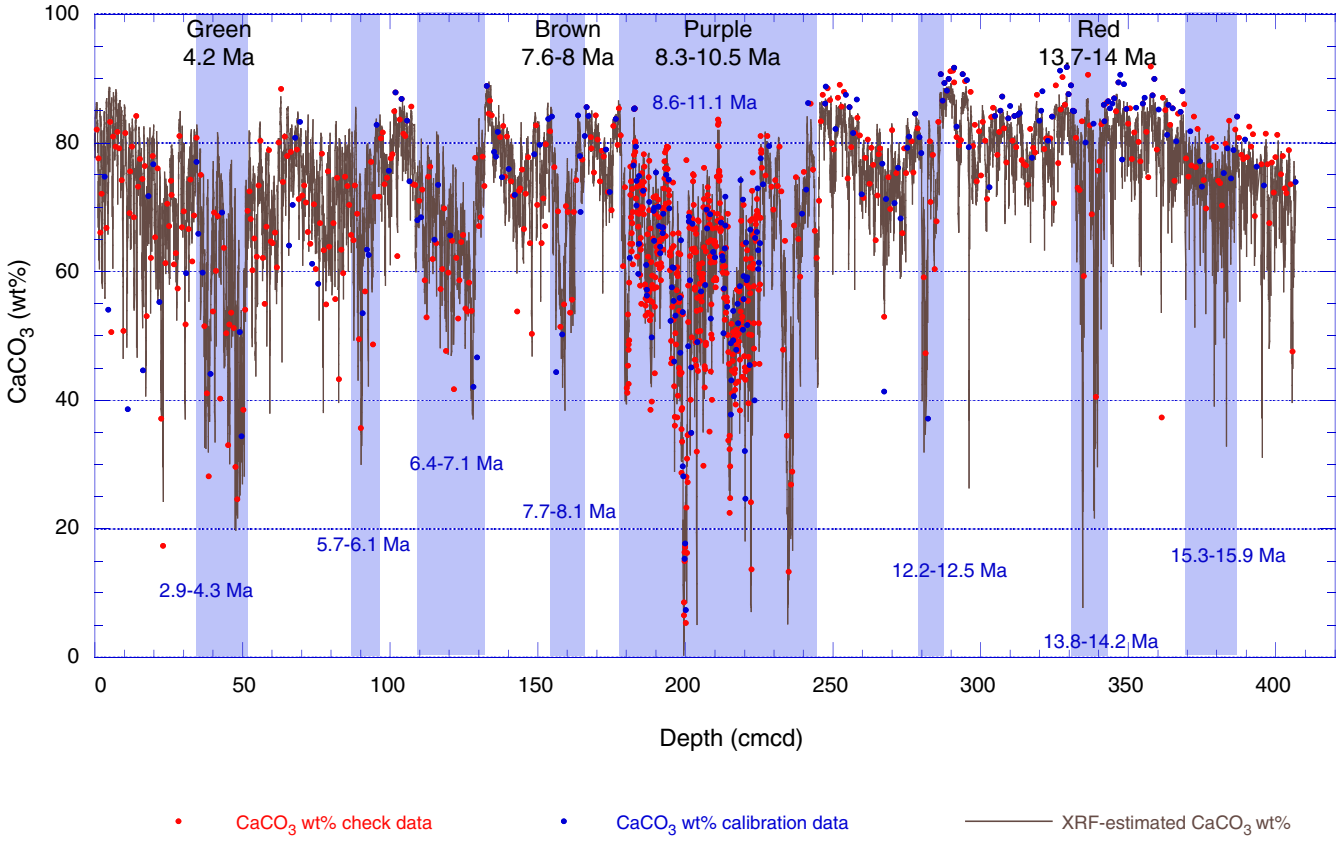

Table T1. Site U1338 discrete $CaCO_3$ analyses from Stockholm University.

Hole, core, section, interval (cm)	Meters below seafloor CSF-A (m)	Offset (m)	Meters composite depth CCSF-A (m)	Compressed meters composite depth CCSF-B (m)	$CaCO_3$ calibrated wt%
321-					
U1338A-1H-1, 45	0.45	0.04	0.49	0.44	82.1
U1338A-1H-1, 120	1.20	0.04	1.24	1.12	77.7
U1338A-1H-2, 45	1.95	0.04	1.99	1.80	66.1
U1338A-1H-2, 96	2.46	0.04	2.50	2.26	72.1
U1338B-1H-3, 45	3.45	0.00	3.45	3.12	74.8
U1338B-1H-3, 120	4.20	0.00	4.20	3.79	66.8
U1338B-1H-4, 45	4.95	0.00	4.95	4.47	54.1
U1338B-1H-4, 120	5.70	0.00	5.70	5.15	83.3
U1338A-2H-2, 45	4.65	1.48	6.13	5.54	50.6
U1338A-2H-2, 120	5.40	1.48	6.88	6.21	81.0
U1338A-2H-3, 45	6.15	1.48	7.63	6.89	79.5
U1338A-2H-3, 120	6.90	1.48	8.38	7.57	81.8
U1338A-2H-4, 45	7.65	1.48	9.13	8.25	79.1
U1338A-2H-4, 120	8.40	1.48	9.88	8.93	74.3
U1338A-2H-5, 45	9.15	1.48	10.63	9.60	50.8
U1338A-2H-5, 120	9.90	1.48	11.38	10.28	81.6
U1338A-2H-6, 45	10.65	1.48	12.13	10.96	38.6
U1338A-2H-6, 120	11.40	1.48	12.88	11.64	69.1
U1338B-2H-3, 120	11.80	1.29	13.09	11.82	75.6
U1338B-2H-4, 45	12.55	1.29	13.84	12.50	79.4
U1338B-2H-4, 120	13.30	1.29	14.59	13.18	68.5
U1338B-2H-5, 45	14.05	1.29	15.34	13.86	84.2
U1338B-2H-5, 120	14.80	1.29	16.09	14.53	73.2
U1338B-2H-6, 45	15.55	1.29	16.84	15.21	77.5
U1338B-2H-6, 120	16.30	1.29	17.59	15.89	74.5
U1338A-3H-3, 45	15.65	2.23	17.88	16.15	44.6
U1338A-3H-3, 120	16.40	2.23	18.63	16.83	76.5
U1338A-3H-4, 45	17.15	2.23	19.38	17.51	53.0
U1338A-3H-4, 120	17.90	2.23	20.13	18.18	71.8
U1338A-3H-5, 45	18.65	2.23	20.88	18.86	62.1
U1338A-3H-5, 120	19.40	2.23	21.63	19.54	78.0
U1338B-3H-2, 120	19.80	2.07	21.87	19.76	76.7
U1338B-3H-3, 45	20.55	2.07	22.62	20.43	65.4
U1338B-3H-3, 120	21.30	2.07	23.37	21.11	76.0
U1338B-3H-4, 45	22.05	2.07	24.12	21.79	55.3
U1338B-3H-4, 120	22.80	2.07	24.87	22.47	37.1
U1338B-3H-5, 45	23.55	2.07	25.62	23.14	17.4
U1338B-3H-5, 120	24.30	2.07	26.37	23.82	61.3
U1338B-3H-6, 45	25.05	2.07	27.12	24.50	70.5
U1338B-3H-6, 120	25.80	2.07	27.87	25.18	67.1
U1338B-3H-7, 45	26.55	2.07	28.62	25.85	74.2
U1338A-4H-3, 45	25.15	3.62	28.77	25.99	72.0
U1338A-4H-3, 120	25.90	3.62	29.52	26.67	61.1
U1338A-4H-4, 45	26.65	3.62	30.27	27.34	62.9
U1338A-4H-4, 120	27.40	3.62	31.02	28.02	57.4
U1338A-4H-5, 45	28.15	3.62	31.77	28.70	81.1
U1338A-4H-5, 120	28.90	3.62	32.52	29.38	66.9
U1338A-4H-6, 45	29.65	3.62	33.27	30.05	69.4
U1338A-4H-6, 120	30.40	3.62	34.02	30.73	51.8
U1338B-4H-4, 45	31.55	2.66	34.21	30.90	59.7
U1338B-4H-4, 120	32.30	2.66	34.96	31.58	66.6
U1338B-4H-5, 45	33.05	2.66	35.71	32.26	74.3
U1338B-4H-5, 120	33.80	2.66	36.46	32.94	61.6
U1338B-4H-6, 45	34.55	2.66	37.21	33.61	68.7
U1338B-4H-6, 120	35.30	2.66	37.96	34.29	80.8
U1338A-5H-1, 120	32.40	5.40	37.80	34.15	77.1
U1338A-5H-2, 45	33.15	5.40	38.55	34.82	65.8
U1338A-5H-2, 120	33.90	5.40	39.30	35.50	75.1
U1338A-5H-3, 45	34.65	5.40	40.05	36.18	59.9
U1338A-5H-3, 120	35.40	5.40	40.80	36.86	51.5
U1338A-5H-4, 45	36.15	5.40	41.55	37.53	41.0

Meters composite depth follows the updated splice in **Wilkens et al.** (2013). Only a portion of this table appears here. The complete table is available in **ASCII.**

Table T2. X-ray fluorescence (XRF)-estimated $CaCO_3$ wt% along the Site U1338 splice.

Hole, core, section, interval (cm)	Meters below seafloor CSF-A (m)	Meters composite depth CCSF-A (m)	Compressed meters composite depth CCSF-B (m)	$CaCO_3$ NMS	$CaCO_3$ (XRF estimate) wt%
321-					
U1338A-1H-1, 25	0.025	0.065	0.059	87.3	81.5
U1338A-1H-1, 50	0.050	0.090	0.081	85.6	79.7
U1338A-1H-1, 75	0.075	0.115	0.104	86.6	80.7
U1338A-1H-1, 100	0.100	0.140	0.126	85.8	80.0
U1338A-1H-1, 125	0.125	0.165	0.149	87.5	81.7
U1338A-1H-1, 150	0.150	0.190	0.172	85.0	79.1
U1338A-1H-1, 175	0.175	0.215	0.194	87.3	81.5
U1338A-1H-1, 200	0.200	0.240	0.217	87.1	81.3
U1338A-1H-1, 225	0.225	0.265	0.239	83.9	78.1
U1338A-1H-1, 250	0.250	0.290	0.262	83.8	77.9
U1338A-1H-1, 275	0.275	0.315	0.285	87.6	81.8
U1338A-1H-1, 300	0.300	0.340	0.307	90.0	84.3
U1338A-1H-1, 325	0.325	0.365	0.330	91.1	85.4
U1338A-1H-1, 350	0.350	0.390	0.352	90.6	84.8
U1338A-1H-1, 375	0.375	0.415	0.375	91.0	85.2
U1338A-1H-1, 400	0.400	0.440	0.397	91.1	85.4
U1338A-1H-1, 425	0.425	0.465	0.420	91.2	85.5
U1338A-1H-1, 450	0.450	0.490	0.443	91.9	86.2
U1338A-1H-1, 475	0.475	0.515	0.465	92.1	86.5
U1338A-1H-1, 500	0.500	0.540	0.488	92.2	86.5
U1338A-1H-1, 525	0.525	0.565	0.510	92.4	86.7
U1338A-1H-1, 550	0.550	0.590	0.533	90.7	85.0
U1338A-1H-1, 575	0.575	0.615	0.556	91.2	85.5
U1338A-1H-1, 600	0.600	0.640	0.578	91.4	85.7
U1338A-1H-1, 625	0.625	0.665	0.601	90.8	85.1
U1338A-1H-1, 650	0.650	0.690	0.623	90.0	84.2
U1338A-1H-1, 675	0.675	0.715	0.646	91.3	85.6
U1338A-1H-1, 700	0.700	0.740	0.668	91.3	85.6
U1338A-1H-1, 725	0.725	0.765	0.691	90.9	85.2
U1338A-1H-1, 750	0.750	0.790	0.714	92.1	86.4
U1338A-1H-1, 775	0.775	0.815	0.736	92.5	86.8
U1338A-1H-1, 800	0.800	0.840	0.759	91.6	85.9
U1338A-1H-1, 825	0.825	0.865	0.781	91.2	85.5
U1338A-1H-1, 850	0.850	0.890	0.804	88.3	82.5
U1338A-1H-1, 875	0.875	0.915	0.827	89.4	83.6
U1338A-1H-1, 900	0.900	0.940	0.849	89.2	83.4
U1338A-1H-1, 925	0.925	0.965	0.872	89.7	83.9
U1338A-1H-1, 950	0.950	0.990	0.894	87.8	82.0
U1338A-1H-1, 975	0.975	1.015	0.917	88.3	82.5
U1338A-1H-1, 1000	1.000	1.040	0.939	88.0	82.2
U1338A-1H-1, 1025	1.025	1.065	0.962	87.6	81.9
U1338A-1H-1, 1050	1.050	1.090	0.985	89.1	83.4
U1338A-1H-1, 1075	1.075	1.115	1.007	87.9	82.2
U1338A-1H-1, 1100	1.100	1.140	1.030	87.7	81.9
U1338A-1H-1, 1125	1.125	1.165	1.052	84.6	78.8
U1338A-1H-1, 1150	1.150	1.190	1.075	86.2	80.3
U1338A-1H-1, 1175	1.175	1.215	1.098	81.6	75.7
U1338A-1H-1, 1200	1.200	1.240	1.120	83.3	77.4
U1338A-1H-1, 1225	1.225	1.265	1.143	82.9	77.0
U1338A-1H-1, 1250	1.250	1.290	1.165	81.2	75.2
U1338A-1H-1, 1275	1.275	1.315	1.188	72.8	66.6
U1338A-1H-1, 1300	1.300	1.340	1.210	76.0	69.9
U1338A-1H-1, 1325	1.325	1.365	1.233	74.2	68.1
U1338A-1H-1, 1350	1.350	1.390	1.256	79.8	73.8
U1338A-1H-1, 1375	1.375	1.415	1.278	76.1	70.0
U1338A-1H-1, 1400	1.400	1.440	1.301	76.0	69.9
U1338A-1H-1, 1425	1.425	1.465	1.323	75.5	69.4
U1338A-1H-2, 25	1.525	1.565	1.414	67.5	61.2
U1338A-1H-2, 50	1.550	1.590	1.436	80.1	74.1
U1338A-1H-2, 75	1.575	1.615	1.459	80.4	74.4
U1338A-1H-2, 100	1.600	1.640	1.481	70.5	64.3

* = splice point (splice is made using the offsets in **Wilkens et al.,** 2013). NMS = normalized median-scaled. Only a portion of this table appears here. The complete table is available in **ASCII.**